Supporting Information

Size Matters: Cocatalyst Size Effect on Charge Transfer and Photocatalytic Activity

Yifat Nakibli[1], Yair Mazal[2], Yonatan Dubi[2], Maria Wächtler[3]*, and Lilac Amirav[1]*

[1]*Schulich Faculty of Chemistry, Technion – Israel Institute of Technology, Haifa 32000, Israel*

[2]*Department of Chemistry, Ben-Gurion University of the Negev, Israel*

[3]*Leibniz Institute of Photonic Technology Jena, Department Functional Interfaces, Albert-Einstein-Straße 9, 07745 Jena, Germany*

Corresponding Authors' e-mail addresses:

Lilac Amirav: lilac@technion.ac.il, *Maria Wächtler:* maria.waechtler@leibniz-ipht.de

1 PHOTOCATALYST SYNTHESIS

1.1 Synthesis of Cadmium Selenide Quantum Dots (CdSe QDs):

CdSe Seeds were synthesized following Manna L. and co-authors procedure.[1] 60mg of Cadmium Oxide (CdO) 0.280g of Octadecylphosphonic acid (ODPA) and 3.0g of Trioctylphosphine oxide (TOPO) are heated to 150°C in a 25mL three-neck flask flushed under argon, followed by a 1 hour long vacuum stage. Then, again under argon, the solution is heated to 300°C. At this point, 1.5 g of Trioctylphosphine (TOP) is injected into the flask. The temperature is raised to 370°C and the solution is removed from the heating mantle. Upon cooling, at 350-330°C, TOP:Se solution (0.058g Se + 0.360gTOP) is rapidly injected. The reaction time is modified in order to synthesize CdSe dots of different sizes. In this work we used 2.3 nm CdSe seeds with green fluorescent, obtained by removal of the heating mantle immediately after the injection. After the synthesis, the nanocrystals are precipitated with methanol, and are washed by repeated redissolution in toluene and precipitation with the addition of methanol.

1.2 Synthesis of Cadmium Sulfide Seeded Rods (CdSe@CdS):

The procedure for the seeded rods synthesis was adopted from.[2] 0.230 g of CdO, 1.08 g of ODPA, 0.075g of Propylphosphonic acid, and 3.35 g of TOPO were loaded into a 25 mL three-neck flask and heated to 120°C for 30 min under vacuum. The mixture was heated to 320 °C under flowing argon to produce an optically clear solution. After the CdO completely dissolved, the solution was cooled to 120°C and put under vacuum for 2 h for removal of water, after which it was heated to 340°C under flowing Ar. At this time, 1.5 g of TOP was injected and the flask was allowed to return to 340°C. TOP:S was prepared by reacting equimolar amounts of TOP and elemental sulfur under inert atmosphere. 0.65 g TOP:S was injected into the flask at 340 °C, followed after 20 sec by the injection of the CdSe seeds dissolved in 0.50 g of TOP. The CdSe solution was prepared by evaporating 0.3 g (or 300ml) of $5 \cdot 10^{-3}$ M solution of CdSe nanocrystals in toluene and redispersing in TOP (gentle sonication might be necessary). The reaction temperature was adjusted to 320 °C, and the reaction was stopped after 15 min by the removal of the heating mantle and the injection of 4 mL of anhydrous toluene. The nanorods were isolated and cleaned by a few repeatable steps of precipitation and redissolution using toluene/hexane/chloroform as solvent and isopropanol/methanol as nonsolvent (10:7 solvent to

nonsolvent ratio), with the alternating addition octylamine and nonanoic acid (about 1-2 ml). Precipitation was achieved by centrifugation for 20-30 min under 4000 rpm.

Modifications to this synthetic procedure allow for control of nanorod length and diameter. The length of the rods could be controlled by the injection of different amounts of CdSe dots with more dots producing shorter rods. Also, the reaction time could be changed to control rod length; longer growth times produce longer rods. Finally, the diameter and length of the rods could be controlled by the amount of TOP:S injected into the reaction; more TOP:S produces longer and skinnier rods.

Rods were synthesized using a 2.3 nm CdSe seed, and with length of 49.1±6.8 nm.

1.3 Colloidal Growth of Nickel Metal Tips on CdSe@CdS Nanorods:

The procedure for the seeded rods synthesis was performed according to a protocol of nickel nanoparticles synthesis with slight modifications.[3] 4 ml of trioctyl phosphine was loaded into a 25 mL three-neck flask and heated to 180°C under Argon flow. A solution of Nanorods:TOP was prepared by precipitating 2.5 ml of 45 mM seeded rod solution and dissolving it in 0.5 nm TOP. This solution was injected and the flask temperature was allowed to return to 180°C. A second solution was prepared by dissolving 0.05 – 0.26 g Ni (acetylacetonate) in 2 ml oleyl amine at 130°C. This solution was injected into the reaction after temperature recovered to 180°C. Removal of the heating mantle and quenching of the flask in a water bath stopped the reaction after 15-30 min. For low Ni concentration of 0.05 g Ni precursor, all reactants were loaded together and time measurement started when temperature reached 160°C. The nanorods were isolated and cleaned by a few repeatable steps of precipitation and redissolution using toluene as solvent and isopropanol/methanol/ethanol as nonsolvent (10:5 solvent to nonsolvent ratio). Precipitation was achieved by centrifugation for 20-30 min under 4000-8000 rpm.

Modifications to this synthetic procedure allow for control over Ni tip diameter by varying Ni amount as specified in Table S1. Reaction conditions and statistics are summarized in Table S1:

***Table S1**. Detailed synthesis conditions and the resulting Ni tip size and standard deviation*

Tip size [nm]	Number of tips [%]				$Ni(AcAc)_2$ [g]	Reaction time [min]
	No tips	1	2	Multiple		
2.3±0.5	9	64	27	0	0.05	15
3.05±0.6	9	70	21	0	0.05	20
5.2±0.6	1	72	26	1	0.13	20
8.9±2.6	7	67	26	0	0.26	20
10.1±2.6	22	74	4	0	0.26	30

1.4 Ligand Exchange:

The TOP ligands on the tipped seeded rods were exchanged with 11-mercaptoundecanoic acid (MUA), a polar ligand that allows the particles to be well dispersed and suspended in water. The nickel tipped seeded rods are precipitated from solution (via the addition of non-solvent and the use of centrifuge). Next, 250 mg of 11- mercaptoundecanoic acid are dissolved in 20g of methanol. Tetramethylammonium hydroxidepentahydrate salt is added until solution pH of 11 is obtained. The MUA solution in methanol is added to the particles residue. This should result in a clean brown solution. Next, the particles are precipitated from the methanol using toluene as non-solvent and centrifuging at 6000 rpm. The particles are then redispersed in water.

1.5 Characterization of Particles:

Transmission Electron Microscopy (TEM) and Electron Dispersive Spectroscopy (EDS) were done on a FEI Tecnai G^2 T20 S-Twin TEM, running at 200keV with a LaB_6 electron source and an FEI Supertwin Objective Lens or on a FEI Titan 80-300 KeV S/TEM at 300keV with a field emission gun electron source. Samples for TEM were prepared by either dropping the solution directly or by aerosolized spray onto 300 mesh ultrathin carbon on lacey carbon grids purchased from Ted Pella Inc.

X-ray photoelectron spectroscopy (XPS) was done using a Thermo-VG SIGMA probe. Sample was prepared by drying solution of particles suspended in toluene and allowed to dry on a FTO substrate. Deconvolusion of signals was done using XPS-Peak Version 4.1. The whole signal was shifted based on the position of the C-1s peak, so that it was exactly 284.8eV. The main peak position observed in our deconvoluted signal was obtained at 852.06 eV with two additional peaks at 853.40eV and 855.39eV. Peak positions were compared to literature values in order to identify the Ni state. The main $Ni2P_{3/2}$ peak position match to that reported by Nesbitt *et al* (peak positions of 852.6),[4] and is most likely indicative of **metallic Ni**.[5]

The peaks observed at 853.4 and 855.39 might be attributed to Ni oxide. The presence of a thin Ni oxide shell might also contribute to the observed extended incubation time of the activity for hydrogen production. This oxide shell is likely reduced during the first stages of the catalytic reaction. It should be noted that XPS measurements were preformed on samples that were exposed to air, while TA measurements were preformed in the course of this work on particles suspended in toluene, that were kept under inert conditions.

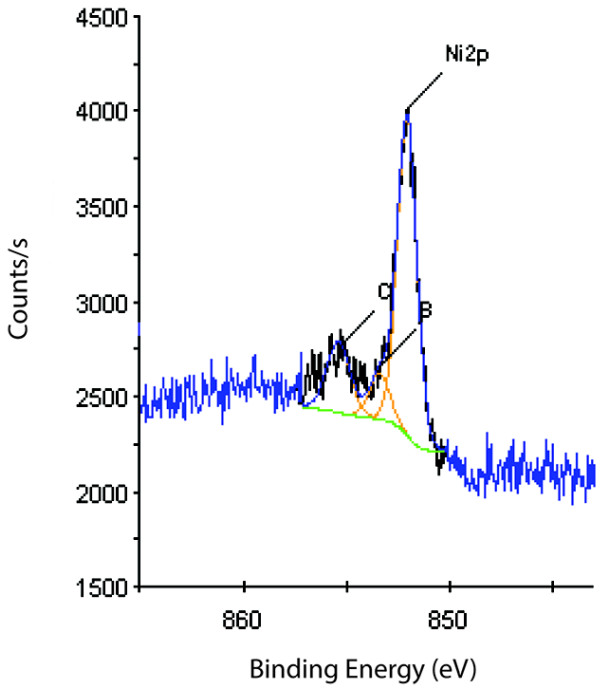

Figure S1. *XPS of the region around the Ni2P peak with corresponds to metallic Ni.*

UV-Vis absorption spectroscopy was done using an Agilent Cary 5000 UV-Vis-NIR spectrophotometer using standard 10 mm fluorometer cuvettes. Spectra were studied using the accompanying Cary WinUV software package. Spectra were used frequently to determine seed size, seed concentration, rod concentration, and the absorbance (Abs) of solutions used for hydrogen production.

Comparing the absorption spectra of the investigated CdSe@CdSe-Ni structures (Figure S2, measured in *toluene*) with the absorption spectrum of the nanorods without metal tips, the characteristic absorption features of the lowest exciton transition between the valence band (VB) edge and the lowest conduction band (CB) level localized in the CdSe core can be found at 557 nm and the features at 463 and 410 nm correspond to the CdS rod based 1Σ ($1\sigma_e$-$1\sigma_h$) and 1Π ($1\pi_e$-$1\pi_h$) exciton transitions, respectively.[6-10] Minor contributions of an excitonic CdS transition stemming from the CdS shell surrounding the CdSe seed is hidden in the red shoulder of the CdS rod band edge transition.[6,11,12] In the Ni-tipped samples superimposed on these excitonic transition features from the semiconductor part of the heteronanostructure are broad absorption features of inter- and intrabrand transitions of the metal nanoparticles spanning from the NIR to the UV region.[13,14]

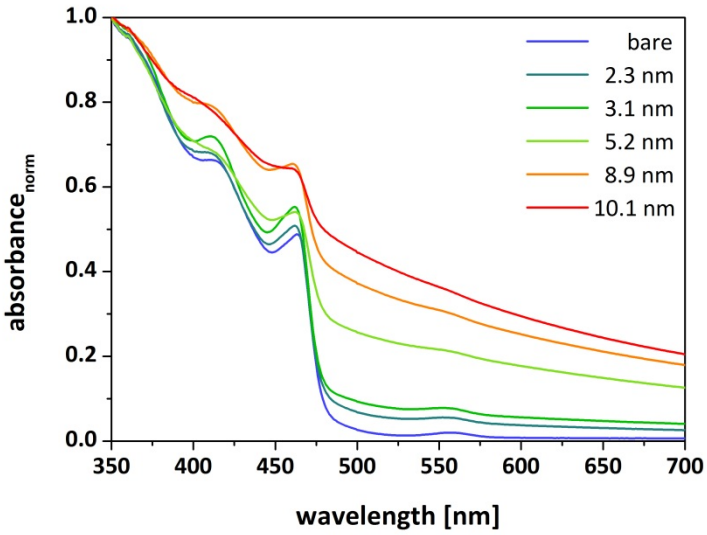

Figure S2. *Normalized absorption spectra of CdSe@CdS nanorods with nickel tips of varying size.*

Photoluminescence (PL) measurements were done using a Fluorolog-3 Fluorimeter, using standard 10 mm fluorimeter cuvettes. Samples were excited at around 450nm and the resulting spectra were measured from 475-800nm. Spectra were studied using accompanying Origin software. The PL Quantum Yield (PL-QY) was determined by comparing the area under the PL spectra (by integration)

that was obtained for the sample with that obtained from solutions of Rhodamine 6G (R6G), a dye with known QY of 95%. The R6G solution (in ethanol) was diluted until it had an identical absorbance to the rods solution at the excitation wavelength chosen, and this absorbance was always kept around 0.1 to avoid overly high or low solution concentrations. Measurements were performed in toluene.

Original rods quantum yield before metal deposition was 44.5%. Photoluminescence is quenched in the metal tipped samples, as is reflected in the respective emission quantum yields. The PL quenching for the different tipped rods is presented in Figure S3.

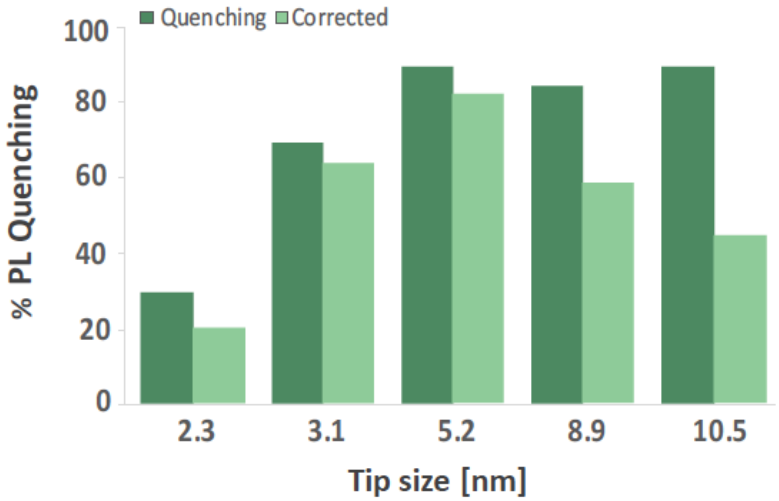

Figure S3. *Photoluminescence quenching for the set of different Ni size tips*

Correction of quantum yields: The weight of the metal contributions increases with the size of the metal tip. Especially the larger metal tips show very strong contributions to the absorption in the visible range. This needs to be taken into account when evaluating quantum yield measurements for both (emission and hydrogen generation).[15,16] When assuming that the absorption spectrum of the tipped nanorods is a simple superposition of the absorption spectrum of the bare nanorod and the absorption spectrum of the Ni nanoparticle at the tip, the contribution of the CdSe@CdS rod to the absorption in the visible range can be estimated by subtraction of the spectrum of the bare rod from the spectrum of the metal tipped samples.[15,16] The resulting difference is supposed to give a spectrum as smooth as possible with increasing absorbance towards shorter wavelengths, what is the characteristic shape of the absorption spectrum of Ni nanoparticles.[13,14] This works sufficiently well in the region of the CdSe seed, which is not in direct contact with the metal nanoparticle, for the CdS band edge transition small deviations can occur,

resulting from the contact region CdS/Ni. Nevertheless, to give an estimate on the portion of the semiconductor part to the overall absorption of the nanostructure the accuracy of this procedure is sufficient. With this information the contribution of the metal tip and the CdSe@CdS rod to the absorbance at a certain wavelength can be estimated.

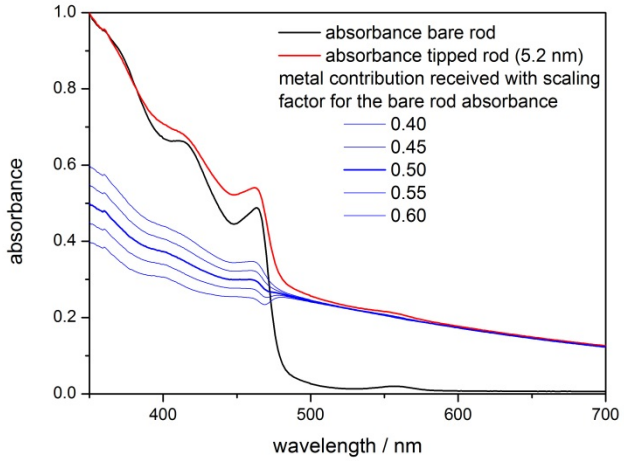

Figure S4. *The contribution of the CdSe@CdS rod to the absorption in the visible range can be estimated by subtraction of the spectrum of the bare rod from the spectrum of the metal tipped samples. The resulting difference is supposed to give a spectrum as smooth as possible with increasing absorbance towards shorter wavelengths, what is the characteristic shape of the absorption spectrum of Ni nanoparticles. From the ratio of the absorbance at 450 nm of the metal tip nm and the complete tipped rod, the percentage of rod absorbance can be calculated. When considering the best scaling factor to be in the range between 0.45 and 0.55, we receive an error interval of 5% for the calculated bare rod contribution (in percent).*

The quantum yields of emission and the quantum efficiency of catalysis are corrected under the assumption that direct excitation of the metal domain does not lead to emission and catalytic activity, hence less photons lead to activation of the sample.

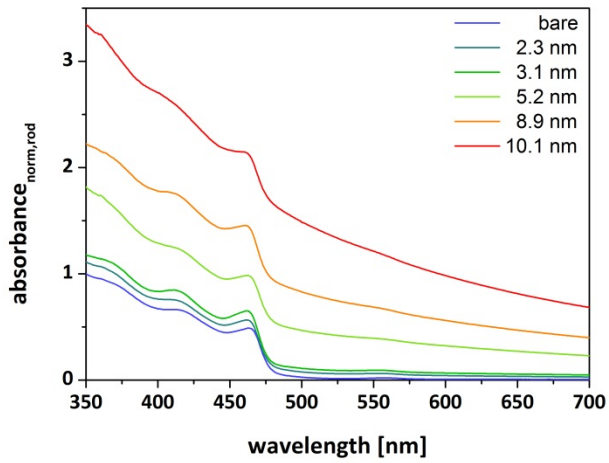

***Figure S5**. Absorption spectra scaled to equal portion of absorbance in the semiconductor part*

***Table S2**. Quantum yields and quantum efficiency of catalysis before and after correction for the internal filter effect of the metal tip. The emission quantum yield upon excitation at 450 nm of the non-tipped nanorods was determined to 44.5%. (*) percentage of the photons of the sample, which lead to excitation the semiconductor part; (**) QY/abs rod@450 nm; QE/abs rod@450 nm.*

Tip Size [nm]	QY Emission	Quenching	QE Catalysis	abs rod @ 450nm*	QY Emission corr**	Quenching**	QE Catalysis corr**
2.3	31.2%	30%	6.2 %	(88±5)%	(35.5±2.0)%	(20±4.5)%	(7.0±0.4)%
3.1	13.4%	70%	11.1 %	(81±5)%	(16.5±1.0)%	(63±2.3)%	(13.7±0.8)%
5.2	4.0%	91%	23.4 %	(46±5)%	(8.7±1.0)%	(81±2.3)%	(50.9±5.5)%
8.9	6.2%	86%	3.5 %	(33±5)%	(18.8±2.8)%	(58±6.3)%	(10.6±1.6)%
10.1	3.9 %	91%	1.2%	(20±5)%	(19.5±4.9)%	(44±11)%	(6.0±1.5)%

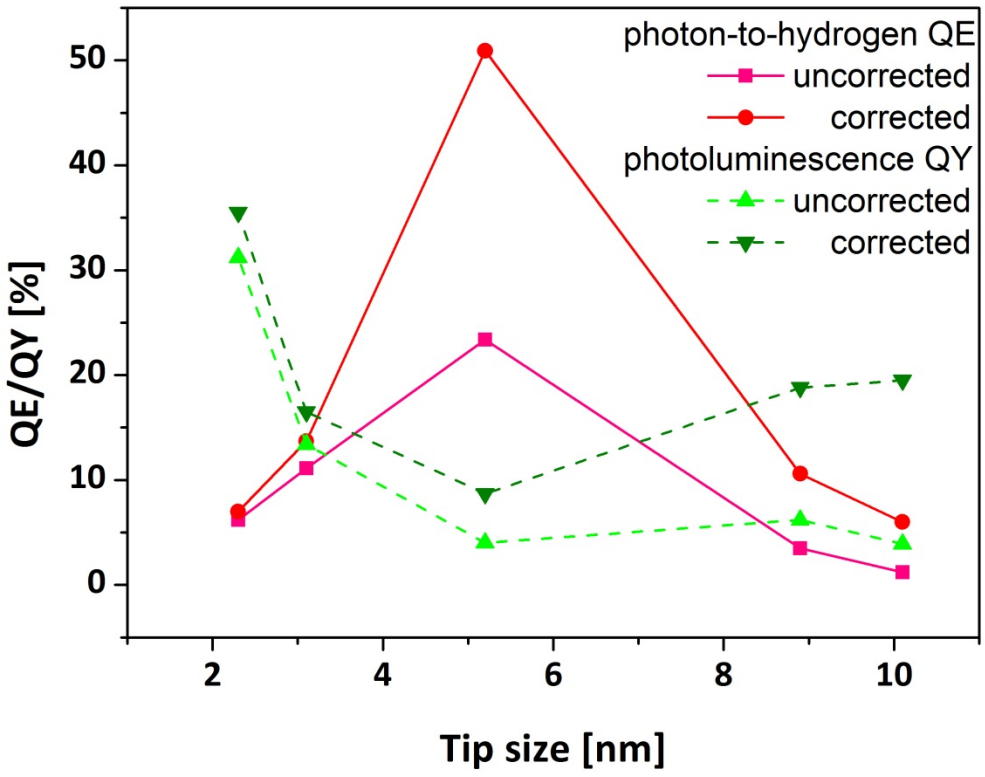

***Figure S6**. Photon to hydrogen conversion efficiencies vs. emission quantum yields uncorrected and corrected for metal tip absorption contributions.*

2 HYDROGEN PRODUCTION MEASUREMENTS

2.1 Experimental Setup and Methodology

Rods solutions were moved to ultrapure water by MUA ligand exchange as close as possible to starting a new measurement, usually less than one hour before the cell was first purged. Samples were diluted using ultrapure water, after which desired amounts of alcohol were added to make 10-11 mL solutions. The gas tight reaction cell (Figure S7) was closed and connected to a 10 mL/min argon line (filtered 99.999% purity) and an Agilent 7890A Series gas chromatograph with a thermal conductivity detector (GC-TCD). Gas was continually flowed through the cell in the dark while the solution was stirred and gas samples were automatically taken every 5 minutes for measurement to monitor the purging process.

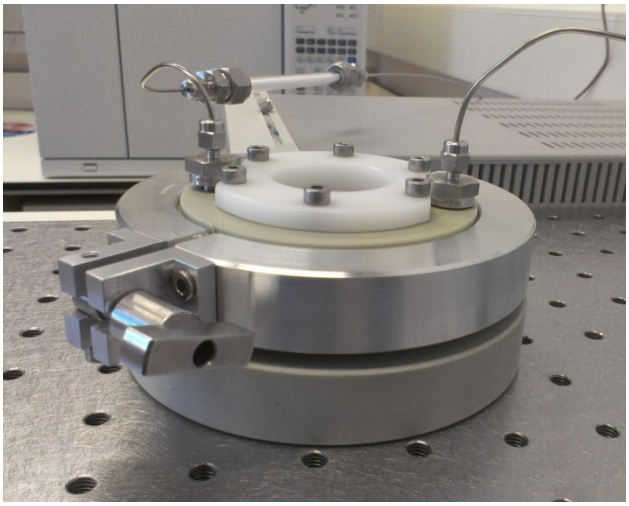

Figure S7*. Photograph of the gas-tight reaction cell with GC seen in the background.*

When the cell was fully purged, a Thorlabs Royal Blue (455nm) high-power LED was switched on to illuminated the sample. The photon flux was calculated by measuring the LED power (which was adjusted to a desired value and measured using a Thorlabs Digital Optical Meter – PM206) assuming all photons had the same wavelength of 455 nm (4.366×10^{-19} Joule/photon). In this adjustment of the power we accounted for the irradiated area over the sample, as well as for the absorption of the reaction cell window and other minor losses in the setup. The LED power used during this work was 50 mW, thus the photon flux (amount of photons per second) is 1.15×10^{17} photons/sec.

2.2 Calculating Quantum Efficiency for Hydrogen Production

Once illuminated, a hydrogen peak was observed, and the integrated area of this peak was used for photocatalytic quantum efficiency (QE%) calculations. The area of the peak obtained from the GC was converted to H_2 production flow rate using prior calibration of the setup. Using the production flow rate, Q[mL/sec], and the ideal gas law, we can calculate the number of hydrogen moles:

For ideal gas: $1\ mol\ gas\ (@\ 25℃) = 24.4\ [L]$

Thus the flow rate with units of mL/sec can be converted to number of moles and later on using Avogadro number to molecules/sec.

At 50mW of power we obtained a flow of 32μL/min, which is equivalent to:

$$\frac{32 \cdot 10^{-6}\left[{}^{L}/_{min}\right]}{24.4\left[{}^{L}/_{mol}\right]} = 1.31 \cdot 10^{-6}\ \left[\frac{mol}{min}\right] = 2.18 \cdot 10^{-8}\ \left[\frac{mol}{sec}\right]$$

Next we can calculate the production rate as number of hydrogen molecules per sec:

$$2.18 \cdot 10^{-8}\ \left[\frac{mol}{sec}\right] \cdot 6.022 \cdot 10^{23}\ \left[\frac{H_2}{ml}\right] = \ 1.31 \cdot 10^{16}\left[\frac{H_2}{sec}\right]$$

Alternatively, the calibration with the electrolysis cell can yield the number of hydrogen molecules per sec directly.

Each hydrogen molecule production requires two electrons, and therefore two photons. Thus the apparent quantum efficiency of the sample is defined as $\mathrm{QE} = \ 2N_{H_2}/N_{h\upsilon}$.

$$QE = \frac{2 \cdot 1.31 \cdot 10^{16}\left[\frac{H_2}{sec}\right]}{1.15 \cdot 10^{17}\ \left[\frac{Photons}{sec}\right]} = \mathbf{0.23}$$

Thus when illumination with a power of 50 mW at 455 nm resulted with hydrogen production rate of 32μL/min we were operating at 23% photons to hydrogen conversion efficiency.

2.3 Discussion Of The Impact Of The Number Of Tips

Dual tipped rods: The presence of two tips in principle should decrease quantum yields for emission, and result with lower efficiency for hydrogen generation[17,18] The presence of two metal tips is not expected to significantly alter the spectroscopic signature of the charge-separated state. The observed kinetics might be altered slightly by influencing the transfer rate via distance differences for charge migration and a higher probability to meet an interface region where interface crossing of the charge can occur. This might result in lower time constants than would be observed for an ensemble consisting of rods 100% functionalized with only one metal tip. However, the portion of dual tipped rods is nearly identical throughout the series (excluding the largest tip size), hence their presence will not alter relative trends.

Bare rods: The presence of bare rods results in higher emission quantum yields than expected from an ensemble of rods that are all functionalized with metal tip(s), and the relative enhancement is estimated in the table below. Based on prior studies, one may assume that bare rods are not contributing to the generation of hydrogen, and the measured hydrogen conversion efficiencies can be corrected for the inactive rods. The observed trend is kept, but is after that correction a bit less pronounced, because the smallest amount non-tipped rods is observed in the most active sample (see table S3). The fitting model in the data analysis of the time-resolved spectroscopy already accounts for nanorods without metal tip.

***Table S3**. QY - emission quantum yields. a) QY(tipped rods)=[QY(sample)-QY(rod)·percentage(non-tipped rods)]/percentage(tipped rods), b) QY/abs rod@450 nm, corrected for internal filter effect of the metal tip, c) not possible to calculate, due to internal filter effect. QE – quantum efficiency for H_2 generation. d) QE(tipped rods)=[QE(sample)/percentage(tipped rods) e) QE/abs rod@450 nm, correction for internal filter effect of the metal tip*

Tip Size nm	Non tipped rods	QY	QY Tipped rods[a]	QY [%] corr[b]	QY Tipped rods corr[b][%]	QE Catalysis	QE tipped rods[d]	QE corr[e] [%]	QE tipped rods corr[e] [%]
2.3	9 %	31.2%	29.8%	35.5±2.0	34.6±2.0	6.2 %	6.8 %	7.0±0.4	7.7±0.4
3.1	9 %	13.4%	10.3%	16.5±1.0	13.7±1.0	11.1 %	12.2 %	13.7±0.8	15.1 ±0.9
5.2	1 %	4.0%	3.6%	8.7±1.0	8.3±1.0	23.4 %	23.6 %	50.9±5.5	51.4±5.6
8.9	7 %	6.2%	3.3%	18.8±2.8	16.8±2.8	3.5 %	3.8 %	10.6±1.6	11.4±1.7
10.1	22 %	3.9 %	-[c]	19.5±4.9	12.4±4.9	1.2%	1.5 %	6.0±1.5	7.7±1.9

3 TRANSIENT ABSORPTION SPECTROSCOPY

3.1 fs Time-Resolved Transient Absorption

The fs time-resolved measurements were performed on as system consisting of a Ti:sapphire amplifier (Legend-Elite, Coherent inc.), producing pulses centred at 795 nm with a repetition rate of 1 kHz. The pump pulses centered at 390 nm and duration of 100 fs are generated by second harmonic generation from the fundamental. The white light continuum between 450 and 700 nm to probe the sample is generated by focussing a part of the fundamental of the amplifier output into a sapphire plate. The pump pulses are delayed with respect to the probe pulses by means of an optical delay stage (maximum delay: 2 ns) and focused into the sample by a lens (f = 1 m). The repetition rate of the pump pulses is reduced to 500 Hz by a mechanical chopper and the polarization of the pump with respect to the probe pulses is set to the magic angle (54.7 °) using a Berek compensator and a polarizer. The white light continuum is split into probe and reference. The probe pulse is focused onto the sample by a concave mirror (f = 500 mm) and spatially overlapped with the pump pulse. Probe and reference are collected by a detection system (Pascher Instruments, AB) consisting of a spectrograph (Acton, Princeton Instruments) equipped with a double-stripe diode array detector. The diode array is read out with the laser repetition rate and the signal (ΔA) is calculated from two consecutive probe pulses, corresponding to pump-on and pump-off conditions.

3.2 Transient Spectra

The transient spectra of the bare rod and the Ni tipped rods (see Figure S8) show the characteristic bleach features of the CdSe and the CdS exciton transitions observable at 555 and 460 nm in agreement with the static absorption spectra. The bleach feature of the exciton transition in the CdS bulb region is as expected weak due to its low volume and hidden underneath the strong bleach of the exciton transition localized in the CdS rod. At early decay times, a positive signal contribution is superimposed on the strong bleach feature in the red shoulder of the exciton bleach localized in the rod, which decays within the first ps parallel to the increase in the signal intensity of the bleach features, and can be assigned to the presence of hot excitons generated in the nanorod upon excitation into higher excitonic transitions at 390 nm.[6,19]

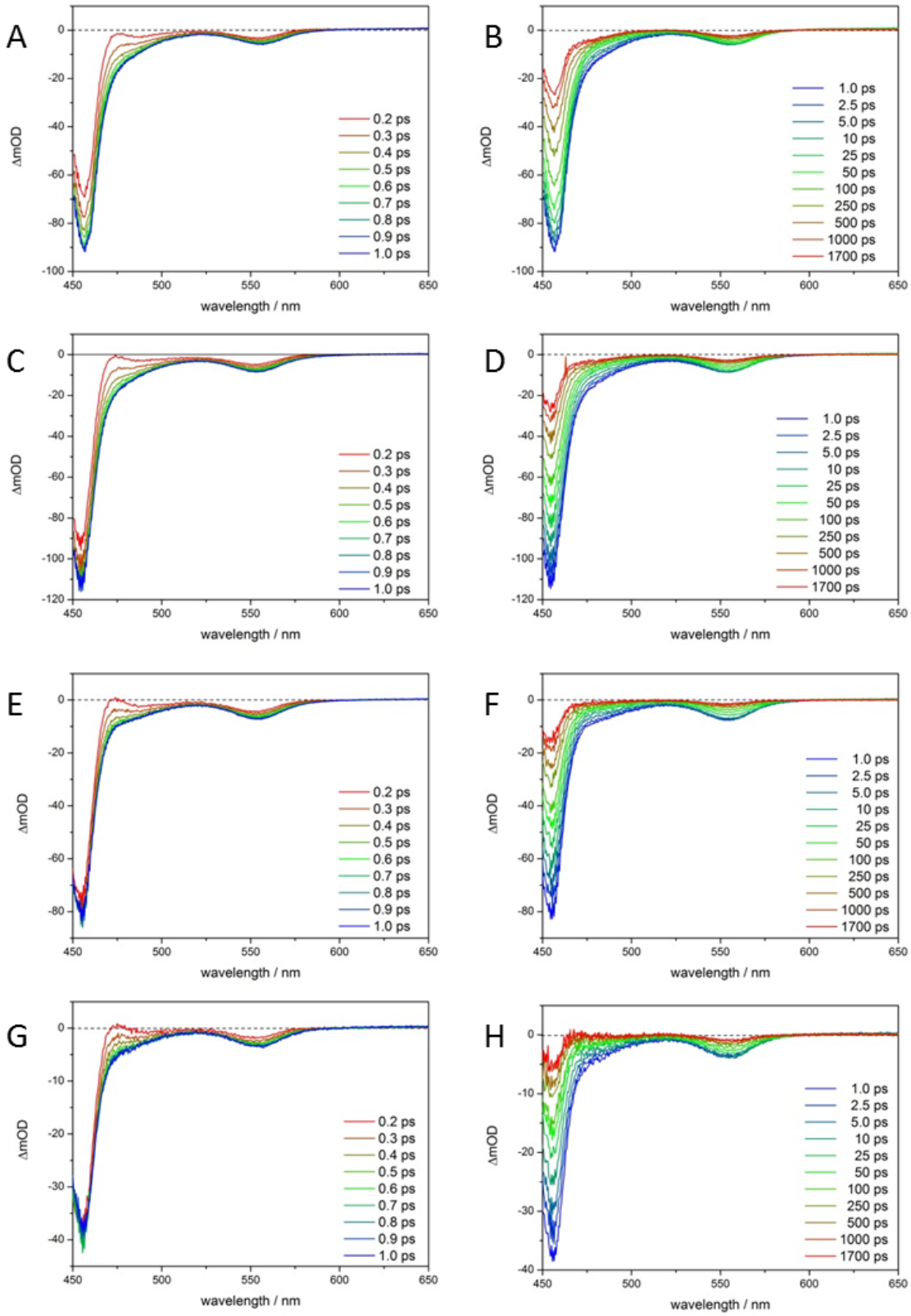
A
B
C
D
E
F
G
H
ΔmOD
wavelength / nm
0.2 ps
0.3 ps
0.4 ps
0.5 ps
0.6 ps
0.7 ps
0.8 ps
0.9 ps
1.0 ps
2.5 ps
5.0 ps
10 ps
25 ps
50 ps
100 ps
250 ps
500 ps
1000 ps
1700 ps

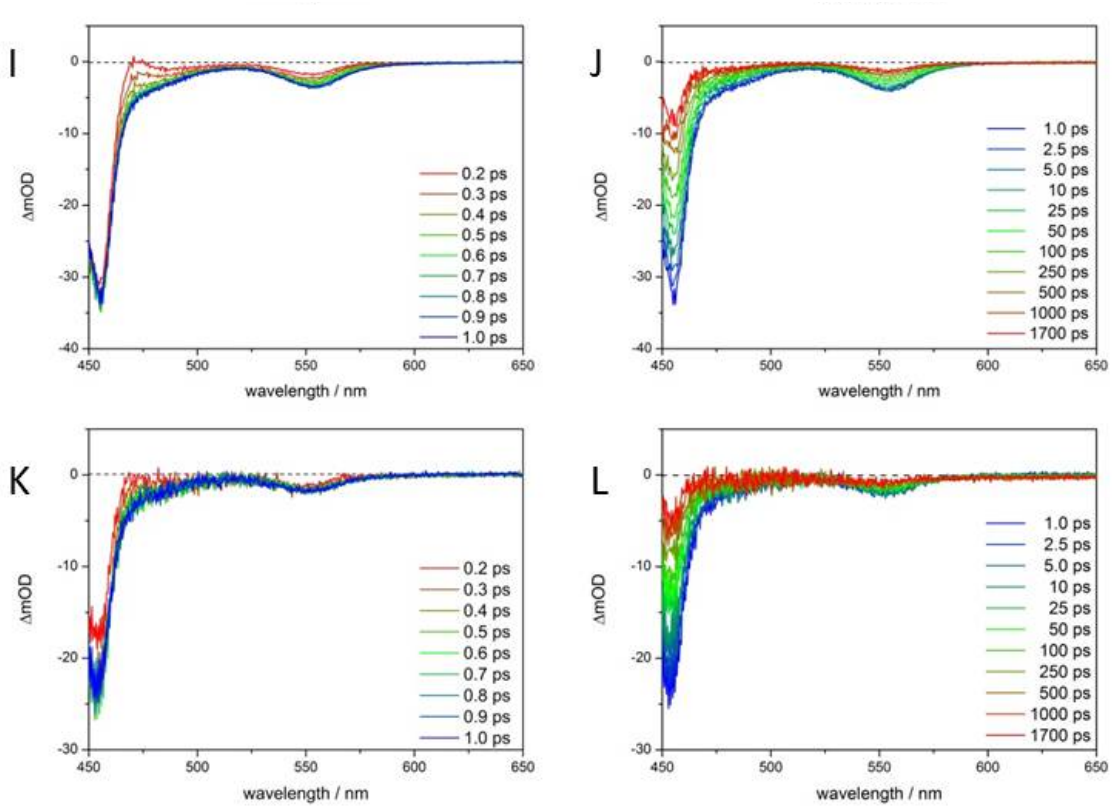

Figure S8. *Transient spectra of the bare rod (A,B), the Ni tipped samples with tip size 2.3 nm (C,D),3.1 nm (E,F), 5.2 nm (G,H), 8.9 nm (I,J), 10.1 nm (K,L) upon excitation at 390 nm.*

3.3 Fitting Results – fs TA data

Bare rod: The temporal evolution at chosen probe wavelengths is fitted by applying a sum of exponential functions:

$$\Delta A(t) = \sum_i A_{fi} e^{\frac{-t}{\tau_{fi}}} + \sum_i A_i e^{\frac{-t}{\tau_i}} + const$$

A_{fi}, τ_{fi} amplitude and time constant of signal formation processes

A_i, τ_i amplitude and time constant of processes describing the signal decay

Table S4. *Fit parameters for the bare rods. (*) amplitudes normalized |A1+A2+A3+const|=1; (**) error 10%, R^2 = 0.999 (458 nm), R^2 = 0.992*

Bare rod	τ_{f1} / ps A_{f1}	τ_{f2} / ps A_{f2}	τ_1 / ps A_1	τ_2 / ps A_2	τ_3 / ps A_3	const.
458 nm CdS	0.24 0.57	-	5.1 -0.09	96 -0.29	726 -0.39	-0.23
555 nm CdSe	0.33 0.71	10 0.02	-	72 -0.30	742 -0.35	-0.35

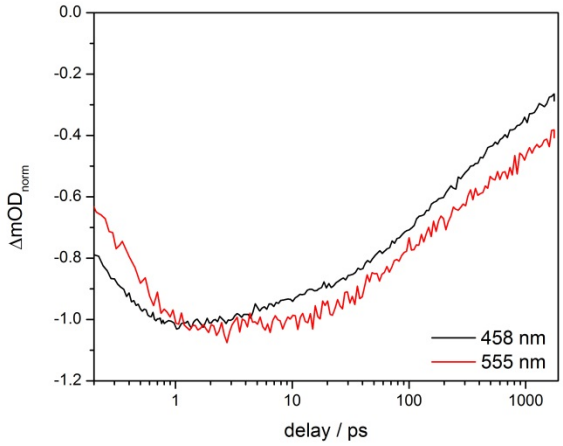

Figure S9. *Comparison of the kinetic traces at probewavelenghts 458 nm and 555 nm probing CdS rod and shell and CdSe excitonic bleach recovery.*

A comparison of the kinetics of the rod localized bleach feature at 458 nm and the seed localized bleach feature at 555 nm probe wavelength revels a similar fast formation of the signal, which can be attributed to an electron relaxation process from the initially excited higher excitonic transitions in both the CdS bulk and the CdSe seed, though the latter is only excited to a low extent. The CdSe seed localized excitonic state kinetics shows a second slower formation component (τ_{f2}= 10 ps) (see Table S4), while the 458 nm rod localized bleach feature is already decaying in this time range. This relates the initial fast decay in the CdS rod bleach and the second growth of the CdSe seed localized exciton signatures to each other and the related process describes the relaxation of an exciton generated in the CdS rod to form excitons that are localized in the CdSe seed driven by the localization of the generated hole in the CdSe seed.[6,11,20] After this process, no interconversion between these two states seems to occur anymore.

Metal-tipped samples: To model the kinetics of the metal tipped rods, the presence of non-tipped rods and only partial electron transfer was taken in to account by including the rod intrinsic relaxation processes into to the fitting function, scaled with a factor C, as determined by measurement of a sample of non-functionalized nanorods. The formation time, hence the relaxation from hot excitons to the band edge states is assumed to be independent of the absence or presence of the metal tip.

$$\Delta A(t) = A_{f1}e^{\frac{-t}{\tau_{fi}}} + \sum_j A_{etj}e^{\frac{-t}{\tau_{etj}}} + C * \left(\sum_i A_i e^{\frac{-t}{\tau_i}}\right) + const$$

A_{fi}, τ_{fi} amplitude and time constant of signal formation processes

A_i, τ_i amplitude and time constant of processes describing the signal decay in the bare rod

A_{etj}, τ_{etj} amplitude and time constant of electron transfer processes

C factor for scaling the rod intrinsic relaxation processes

Table S5. *fit parameters for Ni tipped samples probed at 458 nm, simultaneous fit for the kinetics of all samples with different tip sizes (same time constants for complete dataset),* $R^2 = 0.988$

Charge separation	τ_{f1} / **ps**	τ_{et1} / **ps**	τ_{et2} / **ps**		
	0.24±0.04	1.6±0.3	16.6±1.6		
	A_{f1}	A_{et1}	A_{et2}	**C**	**Const.**
2.3 nm	0.47±0.07	-0.10±0.03	-0.16±0.02	0.72±0.02	-0.16±0.01
3.1 nm	0.49±0.06	-0.15±0.03	-0.19±0.02	0.69±0.02	-0.11±0.01
5.2 nm	0.33±0.06	-0.24±0.03	-0.30±0.02	0.46±0.02	-0.10±0.01
8.9 nm	0.38±0.06	-0.13±0.03	-0.13±0.02	0.70±0.02	-0.18±0.01
10.5 nm	0.36±0.06	-0.21±0.03	-0.10±0.02	0.69±0.02	-0.13±0.01

Table S6. *Fit parameters for Ni tipped samples probed at 555 nm, simultaneous fit for the kinetics of all samples with different tip sizes (same time constants for complete dataset), R^2 = 0.932 (determined from a fit including the data with largest tip size with low signal to noise ratio, without the data with the largest tip size R^2= 0.989, error for the parameters from this fit are given in brackets).*

Charge separation	**τ_{f1} / ps**	**τ_{f2} / ps**	**τ_{et3} / ps**		
	0.34±0.2(0.1)	0.89±0.4(0.2)	34.5±3.7(1.6)		
	A_{f1}	**A_{f2}**	**A_{et3}**	**C**	**Const.**
2.3 nm	0.40±0.23(0.13)	0.16±0.26(0.14)	-0.19±0.03(0.01)	0.61±0.05(0.02)	-0.21±0.01(0.01)
3.1 nm	0.46±0.20(0.11)	0.14±0.26(0.13)	-0.34±0.03(0.01)	0.54±0.06(0.02)	-0.14±0,01(0.01)
5.2 nm	0.34±0.31(0.16)	0.22±0.31(0.16)	-0.29±0.03(0.01)	0.58±0.05(0.02)	-0.14±0.01(0.01)
8.9 nm	0.41±0.24(0.13)	0.16±0.27(0.14)	-0.20±0.03(0.01)	0.60±0.05(0.02)	-0.21±0.01(0.01)
10.5 nm	0.36±0.43	0.31±0.38	-0.18±0.03	0.56±0.05	-0.27±0.01

For probe wavelength 555 nm probing the CdSe bleach feature also in the metal tipped samples a second formation time appears, which is much shorter than for the bare rod and in the order of magnitude of the electron injection time from the CdS excitonic state to the metal nanoparticle. This reflects the situation, that the exciton relaxation to the seed occurs in concurrence to electron injection and as localization is slower than the injection, injection limits the timescale on which exciton localization dynamics is observable.

<u>For comparison fit with simple sum of exponential functions:</u>

The observation of electron transfer constants that are non-variant with metal tip size is in contrast to an earlier report, in which the observed acceleration of the decay of the bleach feature with growing metal tip size is explained by a decrease of the time constant for the separation process.[16] In that investigation a simple sum of exponential functions has been applied to fit the bleach decay, and the acceleration in the bleach feature is described by a simple shortening of the decay times in the exponents and increase of the amplitudes included in the model. This fitting model, however, would only allow a determination of charge transfer time constants for samples where every nanorod is bearing (at least) one metal tip, and

charge separation occurs with a yield of 100%. If this is not the case, this model results with averaged time constants that do not distinguish between rod intrinsic and charge separation processes. This is also reflected in the fact that not just one time constant fit to the data is changing in comparison to the non-functionalized rod, but somehow all exponents change (in the cited work decrease) with increasing tip size. When treating our data in a similar manner, we also find a similar effect (see Tables S7 and S8), but for our data, the determined time constants decrease first until 5.2 nm and increase again for larger tip sizes. From this comparison, we concluded that based on this approach it is not possible to derive a clear statement on the values of the time constants of additional processes depopulating the conduction band in the presence of the metal tip (here charge transfer to the metal tip) and their dependency on the tip size. Only a statement on the varying weight of these processes is possible (which of course is related to the time constant for the transfer step), but no exact number can be derived.

The temporal evolution at chosen probe wavelengths is fitted by applying a sum of exponential functions:

$$\Delta A(t) = \sum_i A_{fi} e^{\frac{-t}{\tau_{fi}}} + \sum_i A_i e^{\frac{-t}{\tau_i}} + const$$

A_{fi}, τ_{fi} amplitude and time constant of signal formation processes

A_i, τ_i amplitude and time constant of processes describing the signal decay

Table S7*. fit parameters for the bare rods and Ni tipped samples at 458 nm. (*) amplitudes normalized |A1+A2+A3+const|=1 (**) error 10%*

Bare rod	τ_{f1} / ps A_{f1}	τ_1 / ps A_1	τ_2 / ps A_2	τ_3 / ps A_3	const.	R^2
Bare	0.24 0.57	5.1 -0.09	96 -0.29	726 -0.39	-0.23	0.999
2.3 nm	0.18 0.60	4.8 -0.20	51 -0.26	506 -0.34	-0.19	0.999
3.1 nm	0.21 0.50	3.7 -0.24	40 -0.28	454 -0.34	-0.14	0.997
5.2 nm	0.14 0.58	2.5 -0.27	22 -0.34	325 -0.25	-0.14	0.993
8.9 nm	0.18 0.47	3.6 -0.19	41 -0.24	513 -0.36	-0.20	0.989
10.1 nm	0.21 0.37	4.24 -0.31	55 -0.23	492 -0.24	-0.22	0.966

Table S8. *Fit parameters for the bare rods and Ni tipped samples at 555 nm. (*) amplitudes normalized |A1+A2+A3+const|=1 (**) error 10%, (***) signal to noise ratio is very small, error 30%*

Bare rod	τ_{f1} / ps A_{f1}	τ_{f2} / ps A_{f2}	τ_1 / ps A_2	τ_2 / ps A_3	**const.**	**R^2**
Bare	0.33 0.71	10 0.02	72 -0.30	742 -0.26	-0.35	0.992
2.3 nm	0.43 0.63	2.0 0.06	49 -0.45	759 -0.28	-0.27	0.997
3.1 nm	0.37 0.53	0.96 0.19	33 -0.52	432 -0.29	-0.19	0.996
5.2 nm	0.29 0.35	0.90 0.34	46 -0.53	656 -0.32	-0.15	0.981
8.9 nm	0.31 0.35	0.74 0.36	38 -0.42	650 -0.32	-0.26	0.986
10.1 nm***	0.49 0.22	1.2 0.30	42 -0.42	829 -0.27	-0.31	0.655

3.4 Estimation of Timescale for Exciton and Electron Transport Along the Rod

The following relation between time τ and diffusion length L_d is used to estimate the time necessary for an exciton or electon to move along a certain distance along the rod, with D being the diffusion coefficient:[21] $\frac{L_d^2}{D} = \tau$

The diffusion coefficient D for excitons in CdSe@CdS nanorods has been determined to $2.3 \cdot 10^{-4}$ m^2/s. This result in ~0.5 ps for 10 nm and ~12 ps for 50 nm.

The diffusion coefficient for electrons can be calculated from the electron mobility μ via the Einstein-Smoluchowski relation, with k_b Boltzmann constant, T temperature in K and q electron charge:[21] $D = \mu \frac{k_b * T}{q}$

The electron mobility μ in CdSe@CdS nanorods was determined to 700 cm^2/Vs.[22] From that a diffusion coefficient D of $1.8 \cdot 10^{-3}$ m^2/s is calculated. This results in 0,1 ps for 10 nm and 2,5 ps for 50 nm.

4 THEORETICAL AND COMPUTATIONAL APPROACH

4.1 Basic Model And Calculation

We model the photo-catalytic particle system as a transport system, where the current flow through it is a measure of the reaction rate, and from it the Quantum Efficiency can be estimated. The basic ingredients are:

1 – The continuum states are models by a set of single-particle levels, i.e. the semiconducting valence band and conduction band, as well as the Ni-tip and CdSe states, are considered as a single level, which can be occupied.[16]

2 – The products and reactants are considered as an infinite reservoir of electrons and holes; the chemical potentials are the reaction potentials (i.e. the energy an electron/hole should have in order to initiate the reaction). This allows us to treat the photo-catalytic process as a *transport process*.

4.2 The System

The system is thus model as a 4-level system, very similar to Ref. [16]. (Figure S10). The numerical parameters are listed in Figure S10 and in Table S9. Conceptually different from Ref. [16], here we are not calculating *rates*, but rather *non-equilibrium steady-state current,* treating the reactants as electron/hole reservoirs. We consider three kinds of transitions: radiative transitions responsible for the exciton generation and recombination (thick arrow), non-radiative transitions (dashed lines in Figure S10), which are responsible for the charge separation at the CdS boundaries and losses due to recombination, and the chemical reactions at the Ni tip and CdSe surface (Green curved arrows). The latter transitions are the only transitions which change the particle number, while the former ones are number-conserving. The surrounding solvent acts as "left" and "right" reservoirs, i.e. an infinite source of electrons, and the effective" chemical potentials" for the electrodes are the reaction potentials..

For the calculation we use the rate equation formalism, which is a common tool for calculating transport currents in molecular systems.[23,24] For this aim we need to define the single-particle Hamiltonian, and the transition rates between them. The Hamiltonian is given by $\mathcal{H} = \sum_{n=1}^{4} \sum_{\sigma=\uparrow,\downarrow} \varepsilon_n c_{n\sigma}^{+} c_{n\sigma}$, where $c_{n\sigma}^{+}(c_{n\sigma})$ is the creation (anihilation) operator for an electron in state n (with energy ε_n) and spin σ,

and $n = 1,2,3,4$ correspond to the CdS valence band (1), conduction band (2), CdSe valence band (3) and the Ni-tip state (4) (see Figure S10). The energetic states are given in Table S9.

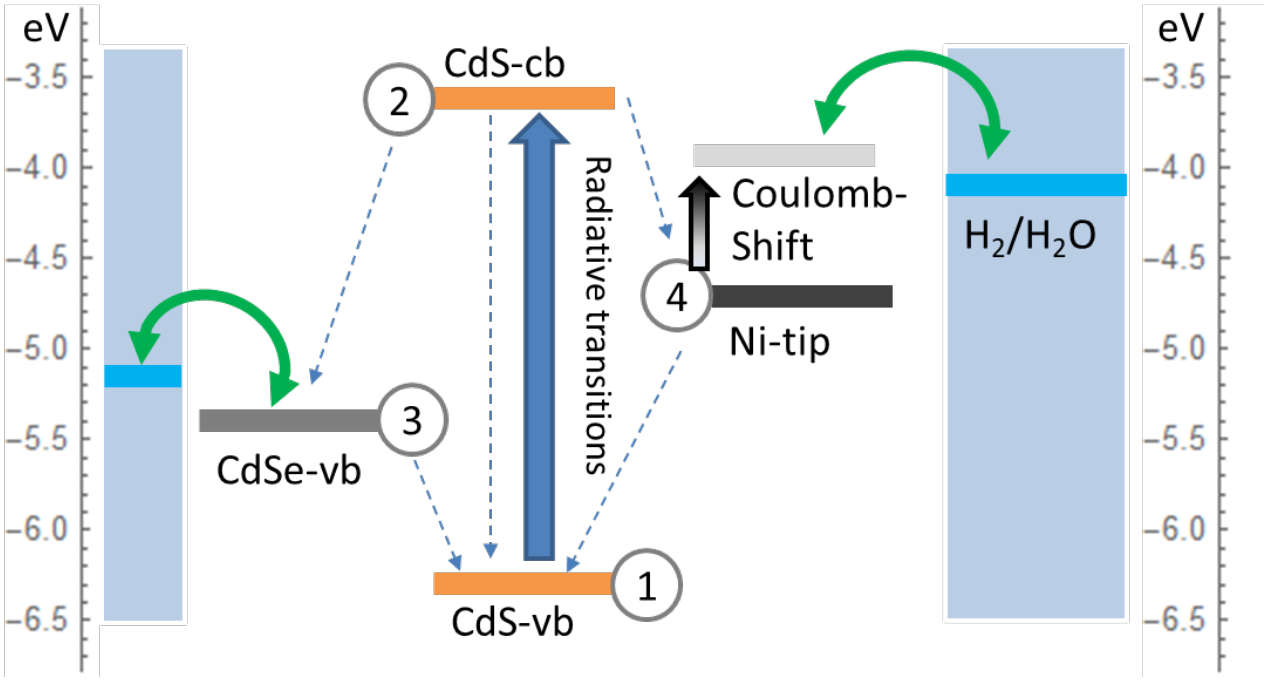

Figure S10. *The 4-level model system. Non-equilibrium steady-state current is calculated*

4.3 The Transition Rates

Once the energetics are determined, we define the Fock many-body states $|N_1, N_2, N_3, N_4\rangle$, where $N_n = 0,1$ is the possible occupations of the state $n = 1,2,3,4$ defined above, a total of $2^4 = 16$ states (we disregard the electron spin, since it plays no role in the processes we discuss). Next, these states are enumerated with an index *iNon*=0,..15, and we define $\mathbf{P} = \{P_0, P_1, \dots, P_{15}\}$ as the probability of the system to be in one of the possible states. P_0 markes the probability of the system to be empty of electrons. We point that basically one should consider the full Fock-space of the system, but since no many-body effects and spin effects are used here, we can limit the system to the single-particle states.

The rate equation is defined as

$$\frac{d}{dt}\mathbf{P} = \mathbf{W} \cdot \mathbf{P} \qquad \text{(S1)}$$

where **W** is the transition-rates matrix, where W_{ij} defines the rate of transition (inverse of the time-scale) from the (Fock) state *i* to state *j* (note that these indices represent Fock states, and not single-particle states, which are noted with n and *m* above).

To estimate the rate matrix, we note that there are several types of terms:

1. Non-Radiative/interface transitions, which connect states with the same number of electrons at different sites. The general form of these transition rates is $\Gamma_{i\to j} = \kappa_{ij} f_D\left(\frac{\Delta E_{ij}}{k_B T}\right)$ where $\kappa_{ij} = \frac{1}{\tau_{ij}}$ is a rate to cross the interface between the states *i* and *j*, ΔE_{ij} is the energy difference, $k_B T$ is the system temperature and $f_D(E) = \left(\exp\left(\frac{\Delta E_{ij}}{k_B T}\right) + 1\right)^{-1}$ is the Fermi function. κ_{ij} is determined by the physical properties of the interface, including wave-functions overlap, disorder and roughness etc., and is a phenomenological parameter.
2. Radiative transition between the CdS valence band and conduction band, $W_{1\to 2}$, which are proportional to the absorbed photon flux γ_{ph} (photons per second which are converted into an exciton pair). Stimulated absorption $W_{1\to 2}$ and emission $W_{2\to 1}$ are connected via detailed balance.[23]
3. Reaction transitions, which are related to the reaction potentials of the different reactions. For instance, for the water-splitting reaction ("right electrode"), this rate will take the form $\Gamma_R = \kappa_R f_F(E_{\mathrm{Ni}} - \mu_R)$, where κ_R is a "bare" rate at which electrons can cross the interface between the Ni-tip and the water molecules, $f_F(\epsilon) = \frac{1}{1+\exp\left(\frac{\epsilon}{k_B T}\right)}$ is the Fermi function, E_{Ni} is the energy level of an electron in the Ni-tip, and μ_R is the water-splitting reaction potential.

Mathematically, the three transitions above are described via the many-body operators $\hat{O} = c_n^+ c_m$, $c_2^+ c_1$ and c_3^+, c_4 for the diffusive, photoexcitation and reaction transitions. The transition matrix elements are defined by $W_{ij} = \Gamma_{ij}\langle i|\hat{O}|j\rangle$ with the rates constants defined above.

4.4 Accounting For Size Effects

As described in the main text, there are two independent processes that we take into account to describe the size effects.

The first effect is the Coulomb blockade, which has been discussed in this context here.[25] We assume he Ni-tip may be charged, and therefore an electron that tries to occupy the tip, will feel a Coulomb-shifted energy level, $\varepsilon_2 = \epsilon_{Ni} + U_c$, where ϵ_{Ni} is the bare energy, and U_c is a Coulomb charging energy, basically an "energy penalty" an electron has to pay in order to occupy the confined space of the Ni tip. Since is originates in Coulomb repulsion, its functional form is $U_c \sim \frac{\alpha}{r}$, where $\alpha = \frac{e\, Z_{eff}}{4\pi\epsilon_0\, \epsilon_r}$ is a system-specific constant, which encodes the properties of the nanoscale Ni tip, including the effective charge Z_{eff} and the Ni tip permitivity (dielectric constant) ϵ_r .

The second, competing, effect, is the reduction of the Schottky barrier with decreasing size, as reported in, e.g., [26]. The mechanism for this reduction is as follows. The Schottky barrier is a result of the local field that is formed between the semiconductor and the metal, due to the formation of a depletion layer. This basically means that electrons diffuse from the metal to the SC, and the resulting charge depletion layer generates a local electric field. Here we suggest that when the particle is small, there are not enough free electrons to traverse the SC-metal interface and create the depletion layer. Therefore the local field is smaller than its bulk value, and correspondingly the barrier is smaller – and the transfer rate from the SC to the metal is larger.

To model this effect, we assume that there is a critical tip radius, $r_c = 6\text{nm}$, above which the Schotky barrier is fully developed. For tips smaller than this, we assume for simplicity that the transfer time is proportional to the volume (i.e. to the total number of electrons). We therefore write:

$$\Gamma_{CdS\to Ni} = \begin{cases} 20\ \text{ns}^{-1}, & r > r_c \\ A - B\, r^2, & r < r_c \end{cases} \qquad \text{(S2)}$$

where $r_c = 6\text{nm}$ and A, B are constants, chosen such thath the rate goes up to ~ 10^2ns^{-1} for small tip radii.

4.5 Current And Quantum Efficiency

Once the transition rate is defined, the probabilities are determined by solving the steady-state rate equation $\mathbf{W} \cdot \mathbf{P} = 0$. Put differently, the probabilities $\mathbf{P}$ are the kernel of the transition rate matrix.

Once the steady-state probabilities are determined, the currents can be calculated via a simple procedure. The calculation proceeds by evaluating the electron density at, say, the Ni tip, n_4. Then, from the definition of current,

$$J_4 = \frac{d}{dt} n_4 \quad . \qquad \text{(S3)}$$

From this expression (whish identically vanishes at steady state) one can recognize the current flowing through the system, which turns out to have a very simple form

$$J = \Gamma_R (n_4 - f_D(\epsilon_4 - \mu_R)) \qquad \text{(S4)}$$

which is evaluated numerically. The quantum yield is the ratio between the total current (i.e. number of electrons per unit time used for the reaction) the effective photon flux (i.e. the number of photons absorbed by the semi-conductor), $QE = \frac{J}{\gamma_{ph}}$

4.6 Numerical Parameters

The model contains many numerical parameters, which signify a set of unknown physical properties. To find these parameters, we used the theory above to calculate the quantum yield as a function of Ni-tip radius, and by comparing the theoretical to the experimental curve, we optimize the model parameters. We take the bare reaction rates from the Ni tip and CdSe to be the smallest time-scale in the system (1fs), since these are not probed in the TA experiments. Table S9 shows the parameters, their physical meaning and their value.

Table S9. *Parameters used in the simulation*

Parameter	ϵ_1[eV]	ϵ_2[eV]	ϵ_3[eV]	ϵ_4[eV]	Φ_L[eV]	Φ_R[eV]
Value	-6.3	-3.6	-5.1	-4.54+$\frac{\alpha}{r}$, $\alpha = 3.6 \frac{\text{eV}}{\text{nm}}$	-5.1	-4.2
description	CdS-vb energy	CdS-cb energy	CdSe-vb energy	Ni-tip energy	oxidation potential	reduction potential

5 REFERENCES

(1) Carbone, L.; Nobile, C.; De Giorgi, M.; Sala, F. D.; Morello, G.; Pompa, P.; Hytch, M.; Snoeck, E.; Fiore, A.; Franchini, I. R.; Nadasan, M.; Silvestre, A. F.; Chiodo, L.; Kudera, S.; Cingolani, R.; Krahne, R.; Manna, L. Nano Lett. 2007, 7, 2942-2950.

(2) Talapin, D. V.; Nelson, J. H.; Shevchenko, E. V.; Aloni, S.; Sadtler, B.; Alivisatos, A. P. Nano Lett. 2007, 7, 2951-2959.

(3) Carenco, S.; Boissiere, C.; Nicole, L.; Sanchez, C.; Le Floch, P.; Mezailles, N. Chem. Mater. 2010, 22, 1340-1349.

(4) Nesbitt, H. W.; Legrand, D.; Bancroft, G. M. Phys. Chem. Miner. 2000, 27, 357-366.

(5) Handbook of X-ray Photoelectron Spectroscopy; Perkin Elmer Corporation.

(6) Wu, K. F.; Rodriguez-Cordoba, W. E.; Liu, Z.; Zhu, H. M.; Lian, T. Q. ACS Nano 2013, 7, 7173-7185.

(7) Sitt, A.; Hadar, I.; Banin, U. Nano Today 2013, 8, 494-513.

(8) Hu, J. T.; Wang, L. W.; Li, L. S.; Yang, W. D.; Alivisatos, A. P. J. Phys. Chem. B 2002, 106, 2447-2452.

(9) Shabaev, A.; Efros, A. L. Nano Lett. 2004, 4, 1821-1825.

(10) Katz, D.; Wizansky, T.; Millo, O.; Rothenberg, E.; Mokari, T.; Banin, U. Phys. Rev. Lett. 2002, 89, 086801

(11) Wu, K. F.; Rodriguez-Cordoba, W.; Lian, T. Q. J. Phys. Chem. B 2014, 118, 14062-14069.

(12) Borys, N. J.; Walter, M. J.; Huang, J.; Talapin, D. V.; Lupton, J. M. Science 2010, 330, 1371-1374.

(13) Li, D.; Komarneni, S. J. Am. Ceram. Soc. 2006, 89, 1510-1517.

(14) Zhang, J.; Lan, C. Q. Mater. Lett. 2008, 62, 1521-1524.

(15) Ben-Shahar, Y.; Banin, U. Top. Curr. Chem. 2016, 374, 54.

(16) Ben-Shahar, Y.; Scotognella, F.; Kriegel, I.; Moretti, L.; Cerullo, G.; Rabani, E.; Banin, U. Nat. Commun. 2016, 7, 10413

(17) Nakibli, Y.; Kalisman, P.; Amirav, L. J. Phys. Chem. Lett. 2015, 6, 2265-2268.

(18) Simon, T.; Carlson, M. T.; Stolarczyk, J. K.; Feldmann, J. ACS Energy Lett. 2016, 1, 1137-1142.

(19) Wu, K.; Zhu, H.; Liu, Z.; Rodríguez-Córdoba, W.; Lian, T. J. Am. Chem. Soc. 2012, 134, 10337-10340.

(20) O'Connor, T.; Panov, M. S.; Mereshchenko, A.; Tarnovsky, A. N.; Lorek, R.; Perera, D.; Diederich, G.; Lambright, S.; Moroz, P.; Zamkov, M. ACS Nano 2012, 6, 8156-8165.

(21) Hodes, G.; Kamat, P. V. J. Phys. Chem. Lett. 2015, 6, 4090-4092.

(22) Kunneman, L. T.; Zanella, M.; Manna, L.; Siebbeles, L. D. A.; Schins, J. M. J. Phys. Chem. C. 2013, 117, 3146-3151.

(23) Einax, M.; Dierl, M.; Nitzan, A. J. Phys. Chem. C 2011, 115, 21396-21401.

(24) Bingqian, X.; Yonatan, D. J. Phys.: Condens. Matter 2015, 27, 263202.

(25) Ruffino, F.; Grimaldi, M. G.; Giannazzo, F.; Roccaforte, F.; Raineri, V. Appl. Phys. Lett. 2006, 89, 243113.

(26) Kwon, S.; Lee, S. J.; Kim, S. M.; Lee, Y.; Song, H.; Park, J. Y. Nanoscale 2015, 7, 12297-12301.